



# Spontaneous and Triggered Longitudinal Combustion Instability in a Single-Injector Liquid-Rocket Combustor

Tuan M. Nguyen\* and William A. Sirignano<sup>†</sup>  
*University of California, Irvine, California 92697*

DOI: 10.2514/1.J057743

Spontaneous and triggered longitudinal combustion instability is simulated numerically in a single-injector liquid-rocket engine using a recently developed axisymmetric compressible flow solver. Turbulence is treated using delayed detached-eddy simulation, whereas chemical reactions are modeled using a compressible flamelet progress variable method. The baseline case is an unstable case that exhibits spontaneous instability and simulates well the experimental evidence. Heat loss is then introduced by imposing an isothermal boundary condition on the chamber wall. Various temperature values are used, with spontaneous longitudinal-mode instability still occurring at the higher wall temperature. Stable but inefficient combustion occurs for the lowest wall temperature. Subsequently, triggered instability of the chamber with low wall temperatures is simulated by perturbing the propellant mass flow rates. Unsteady oscillation can be triggered to higher-amplitude limit cycles. The effectiveness of various disturbances as triggers for instability is quantified through the definition of “triggered energy” and an unsteady Rayleigh-index analysis.

## Nomenclature

$C$	=	progress variable
$C_p$	=	specific heat coefficient at constant pressure
$C_\chi$	=	proportionality constant between turbulence and scalar time scales
$c$	=	speed of sound
$E$	=	total energy
$e$	=	total thermal energy
$h$	=	total enthalpy
$k$	=	turbulent kinetic energy
$M$	=	Mach number
$P$	=	probability density function
$Pr$	=	Prandtl number
$p$	=	pressure
$r$	=	radial vector
$Sc$	=	Schmidt number
$t$	=	time
$u$	=	axial velocity
$v$	=	radial velocity
$x$	=	axial/arbitrary vector
$Z$	=	mixture fraction
$Z'^2$	=	mixture fraction variance
$\gamma$	=	specific heat coefficient ratio
$\lambda$	=	coefficient of thermal conductivity
$\mu$	=	dynamic viscosity coefficient
$\tau$	=	viscous stress tensor
$\phi$	=	arbitrary scalar
$\chi$	=	scalar dissipation rate
$\omega$	=	specific turbulence dissipation frequency

## Subscripts

$f$	=	flamelet quantity
$t$	=	turbulent quantity

## Superscripts

$R$	=	Reynolds quantity
$\bar{\phantom{x}}$	=	Reynolds averaged
$\sim$	=	Favre averaged

## I. Introduction

COMBUSTION instability is an acoustical phenomenon in which combustion excites and sustains an unstable pressure oscillation. It occurs in many high-power propulsion systems that propel rockets and airplanes. These systems have a high-energy release rate with relatively low losses, which in turn reinforce acoustical oscillations with very high amplitudes. These oscillations can cause undesirable effects on thrust, and sometimes engine destruction.

Culick [1] identified two types of acoustical combustion instability: driven and self-excited. Driven combustion instability is found mostly in the solid-propellant rocket engine. The instability occurs in which vortex shedding drives kinematic waves of vorticity or entropy to some point of acoustical reflection. The reflected wave then, in turn, causes more noise (vortex shedding). These instabilities have smaller amplitude as compared to the self-excited type.

Self-excited instabilities, on the other hand, are not limited by the energy of initiation; and they can be found mostly in liquid-propellant rockets. Two types of self-excited instabilities can occur: linear and nonlinear behaviors. Linear behavior refers to spontaneous instability. In this case, an oscillation is excited and grows to an unstable high amplitude from a normal noise level. Nonlinear behavior refers to any fluctuations triggered by unusual conditions such as irregular flow rates or large acoustic disturbances. These disturbances need to have sufficient magnitude to overcome the required threshold [2]. Although the classifications refer to two different kinds of instabilities, both exhibit nonlinear behaviors once they are excited. These instabilities can occur in both the transverse and longitudinal directions.

A series of longitudinal combustion instability experiments conducted at Purdue University provides beneficial information for numerical simulation [3–6]. By only testing a model combustion chamber with a single injector, these experiments provide the ability to capture detailed measurements of the mixing and reactions occurring in the injector flowfield. Moreover, a careful injector-combustion chamber acoustical design was taken into consideration so that the system can sustain and amplify any resulting small pressure disturbance (rumbling noise) [3]. The combustor, called continuously variable resonance chamber (CVRC), thus exhibits

Presented as Paper 2018-4948 at the AIAA/SAE/ASEE Joint Propulsion Conference, Cincinnati, OH, 9–11 July 2018; received 18 July 2018; revision received 7 July 2019; accepted for publication 17 July 2019; published online 22 August 2019. Copyright © 2019 by the authors. Published by the American Institute of Aeronautics and Astronautics, Inc., with permission. All requests for copying and permission to reprint should be submitted to CCC at www.copyright.com; employ the eISSN 1533-385X to initiate your request. See also AIAA Rights and Permissions www.aiaa.org/randp.

\*Assistant Specialist, Department of Mechanical and Aerospace Engineering, Member AIAA.

<sup>†</sup>Professor, Department of Mechanical and Aerospace Engineering, Fellow AIAA.

spontaneous instability. Highly unsteady pressure oscillations occur for both liquid JP-8 (first iteration) and gaseous methane (second iteration) as the fuels. Due to its operating conditions in which the ideal-gas law assumption is valid [7], the second iteration of the experiment has been extensively simulated using both axisymmetric and three-dimensional calculations [7–12].

Numerical studies on triggered instability have been very sparse. For the longitudinal mode, existing studies only involve solid-rocket motors. Particularly, Levine and Baum [13] and Baum and Levine [14] numerically studied triggered combustion instability in solid-rocket motors. The authors observed that the pressure oscillations would reach a limiting amplitude that was independent of characteristics (waveform and amplitude) of the initiating disturbance. Furthermore, the oscillations found were a combination of both traveling and standing waves. Wicker et al. [15] studied a nonlinear combustion response with regard to triggering of the longitudinal combustion instability of solid-rocket motors. A parametric examination of the propellant burning rate and its proportionality to pressure and velocity fluctuations leads to classifications of various linear and nonlinear instabilities. Urbano et al. [16] explored the triggering instability in a 42-injector liquid-rocket engine using a high-fidelity large-eddy simulation (LES) coupled with a flamelet combustion model simulation. However, although the instability in the experiment was self-excited, the initial simulation of the same condition was not: possibly due to the coarse mesh. Therefore, the triggering is used out of necessity to match the experimental findings, which raises the question of triggered instability characteristic. On the other hand, triggered transverse instability in a liquid-rocket engine has been numerically studied using a two-dimensional wave equation model by Sirignano and Popov [2] and Popov et al. [17–20]. The disturbances consist of various forms, such as the acoustic wave within the combustion chamber [2], a localized pressure pulse that models a bombing experiment [17], a blockage in one of the rocket motor injector ports [18], and engine acceleration and vibration [20]. Except for the work of Urbano et al. [16], to the best of the authors' knowledge, research regarding triggered longitudinal combustion instability in liquid-rocket engines has been limited to analytical investigations [21–24]. Moreover, previous numerical investigations of triggered instability relied on either a one-dimensional set of governing equations [13,14] or spatial and time-averaging techniques [15] in which an ad hoc combustion response function was used. This paper therefore presents a numerical study of both spontaneous and triggering instabilities that have no assumption on the pressure-combustion response while solving for relevant detailed flowfields in two dimensions.

In this work, a baseline case, which exhibits spontaneous instability, is first simulated using an adiabatic wall boundary condition. This case has been extensively studied in the existing literature [7–9]: both to benchmark against experimental data as well as to study the CVRC instability mechanism. Garby et al. [25] and Harvazinski et al. [26], while using the CVRC configuration, demonstrated the stabilizing effect of imposing heat loss on the combustor wall. Therefore, this paper follows the same approach to stabilize the instability found in the baseline case. Specifically, various wall heat loss levels are introduced to reduce the pressure oscillation amplitude. We subsequently explore whether the chamber exhibits unconditionally stable or conditionally stable (with an unstable limit cycle) behaviors by introducing various levels of perturbation into the flowfield. Unconditionally stable operation means the chamber can dampen any disturbance regardless of its magnitude. An unstable limit cycle means the chamber initially exhibits low-amplitude pressure oscillations but can grow to higher-pressure amplitudes with sufficiently large perturbations. A stable limit cycle usually refers to the high-pressure oscillation magnitude that the flow returns to regardless of the level of the perturbation. The chamber with different isothermal-wall temperatures is triggered using various amplitudes, wave types, and perturbation periods applied to the propellant inlets. This approach mimics a phenomenon in which the combustion chamber exhibits a stable operating condition during ground testing without disruptive events, whereas combustion instability behaviors might be observed in the same rig during flight.

As shown in various calculations of the CVRC experiments [9,10,12], which include either or both three-dimensional (3-D) and axisymmetric simulations, the major instability characteristics occur in the longitudinal direction. Therefore, the neglect of the azimuthal direction is justified. Additionally, Sardeshmukh et al. [27], while using axisymmetric calculations, compared the pressure oscillation amplitude predictions between the GRI-Mech 1.2 detailed chemical kinetic mechanism and a global mechanism [28]. The oscillation amplitude found in the case with detailed kinetics is qualitatively the same as the one predicted by the 3-D calculations with the global mechanism. On the other hand, axisymmetric simulations with the global mechanism underpredicted both the 3-D calculations and the experimental results by at least a factor of two. Due to the large number of simulations needed for a parametric study of the triggering instability, the calculations in this work are performed using a recently developed axisymmetric solver [8] to maintain a low computational cost. The code is a multiblock finite difference solver. Turbulence is modeled using a hybrid Reynolds-averaged Navier–Stokes/LES method, whereas combustion is accounted for using a compressible flamelet progress variable (CFPV) approach. Advection and diffusion terms are discretized using a central differencing scheme. The Jameson–Schmidt–Tukel hybrid second- and fourth-order artificial dissipation terms are added for numerical stability [29]. A four-step Runge–Kutta time integration scheme is implemented. The solver is second-order accurate in space and fourth-order accurate in time. Compared to other existing solvers, the computational cost of the current solver is at least an order of magnitude lower than existing CVRC axisymmetric simulations in terms of core hours per millisecond of physical time [8]. Oscillation amplitude predictions across different stability regimes agree well with experimental results [8]. Correct flame and wave dynamics for different stability regimes are well captured using relatively coarse meshes. The developed solver is thus suitable for large parametric studies such as the one in this work.

In the following sections, the numerical framework including the governing equations, turbulence model, and the flamelet progress variable combustion model are first presented. Results of the baseline adiabatic case, identifying the major instability mechanism, are discussed. We then address the question of stabilizing effects of heat loss through the combustor wall by imposing three different wall temperature values: 1800, 1030, and 600 K. The possibilities of triggered instability are then investigated by perturbing the propellant mass flow rate. The combination of different disturbance amplitudes, durations, and wave types are examined. The triggered instability was achieved for both the 1800 and 1030 K wall temperatures. A definition of triggered energy is established to quantify the combined effects of different triggering parameters. Transient responses of the triggered instability are described by examining the unsteady propellant mass flow rate behavior. In the new unstable dynamic equilibrium, similarities in the flame shape behaviors are found between the self-excited and the triggered instabilities. We find that the perturbations essentially reorganize the combustion process, promoting strong coupling between the flame and acoustical wave that can ultimately overcome the major damping effect of the wall heat loss. Quantification of the acoustic and chemical reaction coupling is provided by the transient Rayleigh-index analysis.

## II. Numerical Framework

### A. Governing Equations

For a multispecies mixture, the Favre-averaged Navier–Stokes equations are written in conservative form, following Ref. [30]:

$$\frac{\partial \rho}{\partial t} + \frac{\partial \rho \tilde{v}_j}{\partial x_j} = 0 \quad (1)$$

$$\frac{\partial \rho \tilde{v}_i}{\partial t} + \frac{\partial \rho \tilde{v}_i \tilde{v}_j}{\partial x_j} = -\frac{\partial p}{\partial x_i} + \frac{\partial (\tau_{ij} + \tau_{ij}^R)}{\partial x_j} \quad (2)$$

$$\begin{aligned} \frac{\partial \bar{\rho} \tilde{E}}{\partial t} + \frac{\partial \tilde{v}_j (\bar{\rho} \tilde{E} + \bar{p})}{\partial x_j} &= \frac{\partial}{\partial x_j} \left[ \tilde{v}_i (\tau_{ij} + \tau_{ij}^R) + \left( \mu + \sigma_k \mu_t \frac{\partial k}{\partial x_j} \right) \right] \\ &+ \frac{\partial}{\partial x_j} \left[ \left( \frac{\lambda}{c_p} + \frac{\mu_t}{Pr_t} \right) \frac{\partial \tilde{h}}{\partial x_j} \right] \end{aligned} \quad (3)$$

where  $\rho$  is the mean density, and  $u_i$  is the velocity in the  $x_i$  direction. Also,  $p$  is the mean pressure;  $\mu$  and  $\mu_t$  are the molecular and turbulent viscosities;  $\lambda$  and  $C_p$  are the heat conduction and constant specific heat coefficients; and  $\tau_{ij}$  and  $\tau_{ij}^R$  are the molecular and turbulent viscous stress tensors, respectively:

$$\begin{aligned} \tau_{ij} &= \mu \left( \frac{\partial \tilde{v}_i}{\partial x_j} + \frac{\partial \tilde{v}_j}{\partial x_i} - \frac{2}{3} \frac{\partial \tilde{v}_k}{\partial x_k} \delta_{ij} \right) \\ \tau_{ij}^R &= \mu_t \left( \frac{\partial \tilde{v}_i}{\partial x_j} + \frac{\partial \tilde{v}_j}{\partial x_i} - \frac{2}{3} \frac{\partial \tilde{v}_k}{\partial x_k} \delta_{ij} \right) \end{aligned} \quad (4)$$

The total energy  $\tilde{E}$  has the form of

$$\tilde{E} = \frac{1}{2} \left( \sum_{j=1}^n \tilde{v}_j \tilde{v}_j \right) + k + \tilde{e} \quad (5)$$

where  $n$  is the number of dimensions. The first term on the right side is the mean flow kinetic energy. The second term is the turbulence kinetic energy  $k$ . Also,  $\tilde{e}$  is the total thermal energy, which includes the sensible and chemical energies. Enthalpy  $\tilde{h}$  is related to the total thermal energy as  $\tilde{h} = \tilde{e} + (\bar{p}/\bar{\rho})$ . For high-pressure combustion, the ideal-gas law is assumed ( $p = \rho R \tilde{T}$ ), where  $R$  is the specific gas constant. The turbulent Schmidt  $Sc_t$  and Prandtl  $Pr_t$  numbers are assumed to be constant at 0.9 [30].

## B. Turbulence Model

Here, the delayed detached-eddy simulation (DDES) model is based on the 2006 Wilcox  $k - \omega$  model [31]. The conservative form of the governing equations for the turbulence kinetic energy  $k$  and the inverse time scale of the large-scale motion  $\omega$  are written as follows [31]:

$$\begin{aligned} \frac{\partial \bar{\rho} k}{\partial t} + \frac{\partial (\bar{\rho} \tilde{v}_j k)}{\partial x_j} &= (\tau_{ij} + \tau_{ij}^R) \frac{\partial \tilde{v}_i}{\partial x_j} - \beta^* \bar{\rho} \omega k \\ &+ \frac{\partial}{\partial x_j} \left[ \left( \mu + \sigma_k \frac{\rho k}{\omega} \right) \frac{\partial k}{\partial x_j} \right] \end{aligned} \quad (6)$$

$$\begin{aligned} \frac{\partial \bar{\rho} \omega}{\partial t} + \frac{\partial (\bar{\rho} \tilde{v}_j \omega)}{\partial x_j} &= \frac{\gamma \omega}{k} (\tau_{ij} + \tau_{ij}^R) \frac{\partial \tilde{v}_i}{\partial x_j} - \beta \bar{\rho} \omega^2 \\ &+ \frac{\partial}{\partial x_j} \left[ \left( \mu + \sigma_\omega \frac{\bar{\rho} k}{\omega} \right) \frac{\partial \omega}{\partial x_j} \right] + \frac{\bar{\rho} \sigma_d}{\omega} \frac{\partial k}{\partial x_j} \frac{\partial \omega}{\partial x_j} \end{aligned} \quad (7)$$

where  $\beta^*$ ,  $\beta$ ,  $\sigma_k$ ,  $\sigma_\omega$ , and  $\sigma_d$  are modeling constants. The turbulent viscosity is calculated as  $\mu_t = \bar{\rho} k / \hat{\omega}$ , where  $\hat{\omega}$  is the turbulent frequency corrected by the maximum of  $\omega$  and the flow mean strain rate.

In any version of the detached-eddy simulation (DES) approach, the dissipation term in Eq. (6) (second term on the right side) is modified to exclude any grid-realized contribution in the turbulent viscosity. This can be achieved by using the following mathematical definition [32]:

$$\beta^* \rho \omega k = \rho k^{3/2} / L_T^* \quad (8)$$

where the corrected turbulent length scale is defined as

$$L_T^* = \min(L_T, C_{DES} L_{GRID}) \quad (9)$$

where  $C_{DES}$  is a modeling constant, which has a value of 0.45 in this work.  $L_T$  and  $L_{GRID}$  are the turbulent and grid length scales where  $L_T = k^{1/2} / (\beta^* \omega)$  and  $L_{GRID} = L_T - F_D (L_T - \Delta)$ .  $\Delta$  is the largest grid dimension for the cell. In the traditional DES approach,  $F_D$  has a value of unity. In the DDES approach,  $F_D$  is a hyperbolic tangent blending function that uses the distance of the cell away from the wall as an input [33]. This blending function is used to limit grid arbitrariness because the smallest grid sizes of the mixing shear layer and the wall boundary layers are the same in this work.

## C. Compressible Flamelet Progress Variable Approach

In the CFPV approach [34], presumed probability density functions (PDFs) are used to relate the laminar flamelet solutions in the mixture fraction space to their Favre-averaged/mean counterparts. The  $\beta$  PDF is assumed for the mixture fraction, whereas the Dirac  $\delta$  PDF is assumed for both the progress variable and pressure. The Favre-averaged thermochemical quantities  $\tilde{\psi}_i$  at each pressure value are preprocessed as lookup libraries using the convolution

$$\tilde{\psi}_i(\tilde{Z}, \tilde{Z}'^2, \tilde{C}, \tilde{p}) = \int_0^1 \int_0^1 \int_{p_o}^p \psi_i(Z, C) \beta(Z, Z'^2) \delta(C) \delta(p) dZ dC dp \quad (10)$$

where  $Z$  is the mixture fraction, and  $C$  is the progress variable. In this work, the progress variable is defined as the total mass fraction of hydrogen ( $H_2$ ) and carbon dioxide ( $CO_2$ ).

During the computational fluid dynamics computation, the transport equations for the mean scalars  $\tilde{Z}$ ,  $\tilde{Z}^2$ , and  $\tilde{C}$  are solved. The mean mixture fraction squared  $\tilde{Z}^2$  is related to the mean mixture fraction  $\tilde{Z}$  and the mean variance  $\tilde{Z}'^2$  as  $\tilde{Z}^2 = \tilde{Z}^2 + \tilde{Z}'^2$ . With the Lewis number equal to one, the transport equations for these scalars are given as

$$\frac{\partial \bar{\rho} \tilde{Z}}{\partial t} + \frac{\partial \bar{\rho} \tilde{v}_j \tilde{Z}}{\partial x_j} = \frac{\partial}{\partial x_j} \left[ \left( \frac{\lambda}{c_p} + \frac{\mu_t}{Sc_t} \right) \frac{\partial \tilde{Z}}{\partial x_j} \right] \quad (11)$$

$$\frac{\partial \bar{\rho} \tilde{Z}^2}{\partial t} + \frac{\partial \bar{\rho} \tilde{v}_j \tilde{Z}^2}{\partial x_j} = \frac{\partial}{\partial x_j} \left[ \left( \frac{\lambda}{c_p} + \frac{\mu_t}{Sc_t} \right) \frac{\partial \tilde{Z}^2}{\partial x_j} \right] - \bar{\rho} C_x \omega (\tilde{Z}^2 - \tilde{Z}^2) \quad (12)$$

$$\frac{\partial \bar{\rho} \tilde{C}}{\partial t} + \frac{\partial \bar{\rho} \tilde{v}_j \tilde{C}}{\partial x_j} = \frac{\partial}{\partial x_j} \left[ \left( \frac{\lambda}{c_p} + \frac{\mu_t}{Sc_t} \right) \frac{\partial \tilde{C}}{\partial x_j} \right] + \tilde{\omega}_C \quad (13)$$

where  $C_x$  has a constant value of 2.0 [30]. Turbulence mixing and turbulence/flame interaction of the mean mixture fraction are modeled by solving Eq. (12), which implicitly describes the variance of the mean mixture fraction  $\tilde{Z}'^2$  [35].

At each time step, the local values of these scalars along with the pressure allow us to retrieve quickly properties such as local compositions, temperature, specific heat  $C_p$ , enthalpy, and thermal diffusivity using pretabulated flamelet libraries.

At the end of each time step, the local values of the Favre-averaged thermal energy  $\tilde{e}$  can be different from the thermal energy  $e_f$  computed from the turbulent flamelet transport equations [Eqs. (11–13)]. However, the local compositions are the same for both quantities. Following Pecnik et al. [30], for a given  $\tilde{e}$  value computed from the Navier–Stokes equations, an expansion around the thermal energy of the flamelet solutions has the form

$$\tilde{e} = e_f + \int_{T_f}^{\tilde{T}} c_v(T) dT = e_f + \int_{T_f}^{\tilde{T}} \frac{R_f}{\gamma(T) - 1} dT \quad (14)$$

where the subscript “ $f$ ” denotes the values of the flamelet solution. The specific heat ratio  $\gamma$  can be expressed as

$$\gamma(\tilde{T}) = \gamma_f + a_\gamma(\tilde{T} - T_f) \quad (15)$$

where  $a_\gamma$  is the local linear expansion coefficient and is tabulated during the preprocessing step as a flamelet library.

Integrating Eq. (14) and solving for  $\tilde{T}$ , we get

$$\tilde{T} = T_f + \frac{\gamma_f - 1}{a_\gamma} (\exp(a_\gamma(\tilde{e} - e_f)/R_f) - 1) \quad (16)$$

For some simulations presented in this work, the isothermal boundary condition is applied on the combustor wall to introduce heat loss to the chamber. At the end of each time step, for a specified wall temperature, the total thermal energy on the combustor wall is calculated from Eq. (16) as

$$\tilde{e}_{\text{wall}} = e_f + \frac{R_f}{a_\gamma} \ln \left[ \frac{a_\gamma}{\gamma_f - 1} (\tilde{T} - T_f) + 1 \right] \quad (17)$$

Equation (17) implicitly introduces heat loss by decreasing the main flow sensible energy and not the chemical reaction energy generated by the flamelet. This approach should be distinguished from the one used by Ma et al. [36], where heat loss was directly introduced into the laminar flamelet formulation.

#### D. CVRC Details

Figure 1 shows the cylindrical computational domain used in this work.

As seen in Fig. 1, the CVRC is essentially a coaxial dump combustor. The oxidizer is injected in the central tube, and fuel is injected in the concentric outer tube. The fuel is methane with a temperature of 300 K. The oxidizer is decomposed hydrogen peroxide with a composition of 58%  $\text{H}_2\text{O}$  and 42%  $\text{O}_2$  by mass. The oxidizer temperature is 1030 K.

The constant mass flow rate inlet boundary condition is implemented using the Navier–Stokes characteristic boundary conditions [37]. To save computational resources, a short-choked-nozzle [38] outlet boundary condition is used instead of an actual convergent–divergent nozzle computational domain. The entrance to throat area ratio is five, based on the CVRC experimental geometry.

### III. Results and Discussions

#### A. Baseline Case

The baseline case for comparison has a 14 cm oxidizer post length with the 38 cm combustion chamber. The chamber walls are adiabatic. The fuel and oxidizer mass flow rates are kept constant at  $\dot{m}_f = 0.027$  kg/s and  $\dot{m}_o = 0.32$  kg/s. The flow is globally fuel lean with an equivalence ratio of 0.8. Nguyen et al. [8] used the coarse mesh with approximately 62,000 grid points to simulate the instability behaviors of the baseline case while validating the current numerical tools. The results are in good agreement with experimental results. Moreover, the solver was able to capture the correct physics in terms of the pressure oscillation amplitude, the mode shape, and time-averaged results as compared to more computationally intensive 3-D simulations. The readers are referred to the work of Nguyen [39] for the complete comparisons.

To further improve the quality of the simulations, a finer mesh is used in this work. The mesh consists of 134,000 grid points. Its

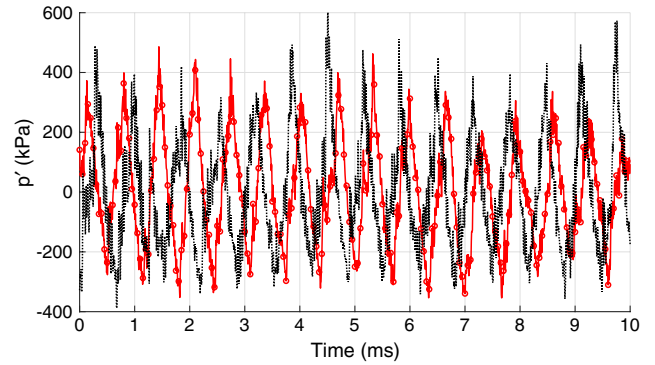


Fig. 2 Pressure signal on the combustor wall at  $x = 38$  cm for the coarse mesh (marker) and fine mesh (no marker).

structure is based on the mesh used in the 3-D calculations of Srinivasan et al. [9]. The smallest radial grid size is 0.05 mm, located around the mixing shear layer or any walls. The smallest axial grid size is 0.4 mm, located both upstream and downstream of the backstep. The maximum grid stretching factor along any direction is 1.03, thus ensuring a high-quality mesh. Figure 2 compares the pressure signal results for the meshes. Both pressure signals are sampled at 200 kHz. There are very little differences between the two meshes used here.

Figure 3 compares the power spectral density results for the pressure signals shown in Fig. 2. For the first mode frequency (F1), the spectral responses are the same. However, there are more distinctive peaks in the second (F2) and third (F3) modes. As seen in these figures, the first three fundamental modes contain almost all the acoustic energy. Therefore, further grid refinement is not performed to retain low computational costs.

The preceding discussion about the mesh size should not be confused with a thorough grid convergence study. In fact, there has been no grid convergence study presented for the CVRC experiment in any existing computations [9–12]. Based on the mean oxidizer jet characteristics and dimensions, the Reynolds number is roughly 400,000. Furthermore, highly nonlinear coupling between the energy release rate and the pressure in such a turbulent flow renders the task of obtaining statistically converged flowfields a challenge that should be addressed in the future, which is not within the scope of this work.

Figure 4a shows the pressure signal for the baseline adiabatic case on the combustor wall at  $x = 37$  cm, which is immediately upstream of the nozzle entrance. This is the same signal as shown in Fig. 2, but it is repeated here for clarity purposes. Limit-cycle behavior is established with a peak-to-peak oscillation amplitude of approximately 600 kPa. This is the most unstable case in the CVRC experiment. Additionally, the mode shape of the entire rocket engine based on the first-mode frequency is plotted in Fig. 4b. At each instant of time, the pressure field at each axial location is first radially averaged, and then it is weighted by the radius to give an average based on cross-sectional area. At each axial location, using a fast Fourier transform, we obtain the modulus response of the first-mode frequency for each pressure signal. A standing half-wave is observed in Fig. 4b. There are two pressure antinodes located immediately downstream of the backstep ( $x = 0$  cm) and at the nozzle entrance

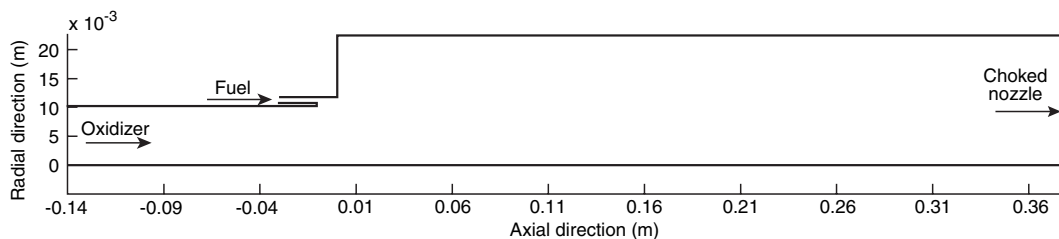


Fig. 1 Computational domain for the CVRC experiments.

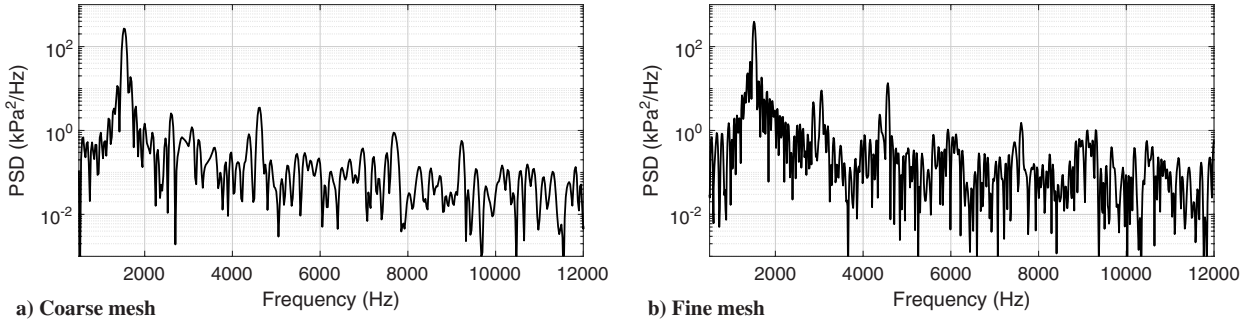


Fig. 3 Power spectral density results for two different mesh sizes.

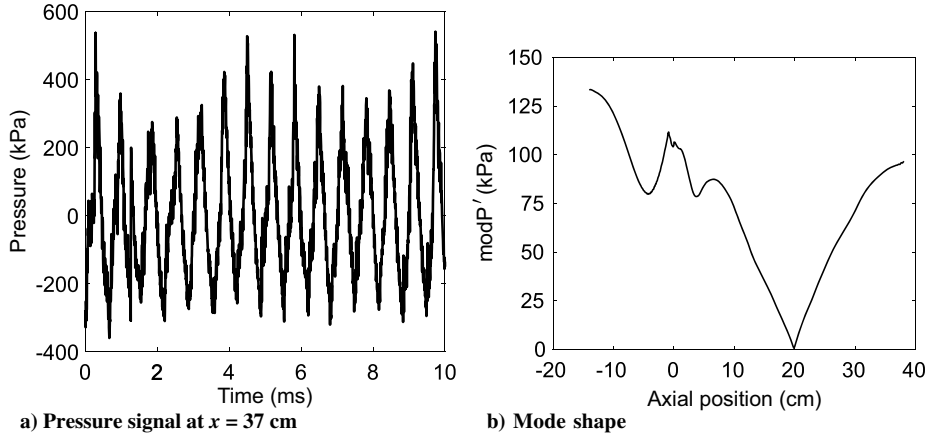


Fig. 4 Instability behaviors of the baseline case.

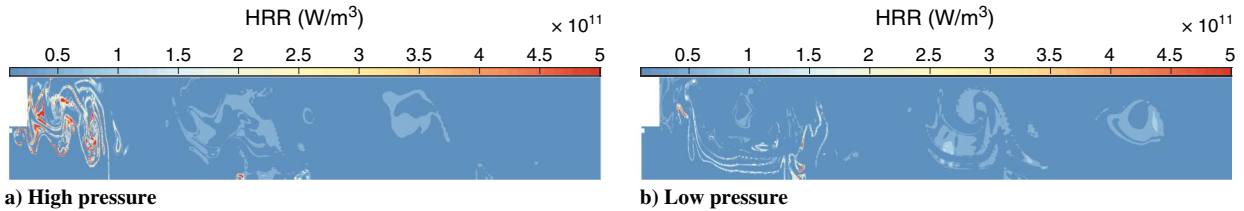


Fig. 5 Instantaneous HRR of the entire combustion chamber at two different times of an unstable cycle.

( $x = 38$  cm). A pressure node is found at the midpoint of the chamber.

Figure 5 shows the transient behavior of the flame occurring inside the combustion chamber. When the pressure at the upstream antinode ( $x = 0-10$  cm) is high, there are intense reactions occurring in this region, as shown in Fig. 5a. In contrast, once the high-pressure wave passes this region, the flame becomes significantly cooler, with its shape changing drastically. This strong flame-acoustic coupling in the upstream pressure antinode is the major factor that leads to highly unstable oscillatory behavior observed in the chamber.

To further confirm and quantify the effects of flame-acoustic interaction, a time-averaged spatially local Rayleigh index [12] is defined as

$$RI = \frac{1}{\tau} \int_{t_0}^{t_0+\tau} \frac{\gamma - 1}{\gamma} p' \dot{\omega}' dt \quad (18)$$

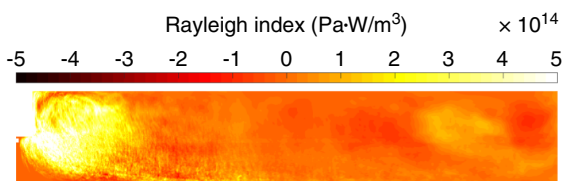


Fig. 6 Rayleigh-index result. The whole chamber is shown with a 3:1 aspect ratio.

where  $p'$  is the local pressure oscillation, and  $\dot{\omega}'$  is the volumetric heat release rate (HRR) oscillation. Figure 6 shows the Rayleigh-index result of the entire combustion chamber. A positive Rayleigh index indicates a strong coupling between the pressure oscillations and the unsteady HRR. A negative Rayleigh index indicates the HRR damping effect on the pressure oscillation. Figure 6 shows a strong correlation between the pressure oscillations and the HRR around the recirculation zone, as well as the mixing layer immediately after the splitter plate. This further confirms the conclusions drawn from comparing Figs. 4 and 5.

### B. Stabilization

For all cases presented in this section, all operating conditions (e.g., propellant thermodynamic properties and mass flow rates), as well as the mesh, are kept the same as in the baseline case. Three different fixed wall temperatures are considered: 1800, 1030, and 600 K. All other parameters are kept the same as the baseline case. For the adiabatic baseline case, the time-averaged temperature on the combustor wall is around 2700 K. Figure 7 shows pressure signals for all cases, which also include the baseline case result for clarity purposes. A significant reduction in oscillation amplitude is immediately achieved from the adiabatic case to the 1800 K case. Lowering the wall temperature from 1800 to 1030 K, and subsequently to 600 K, results in monotonic but moderate decreases in oscillation amplitude as compared to going from the adiabatic case

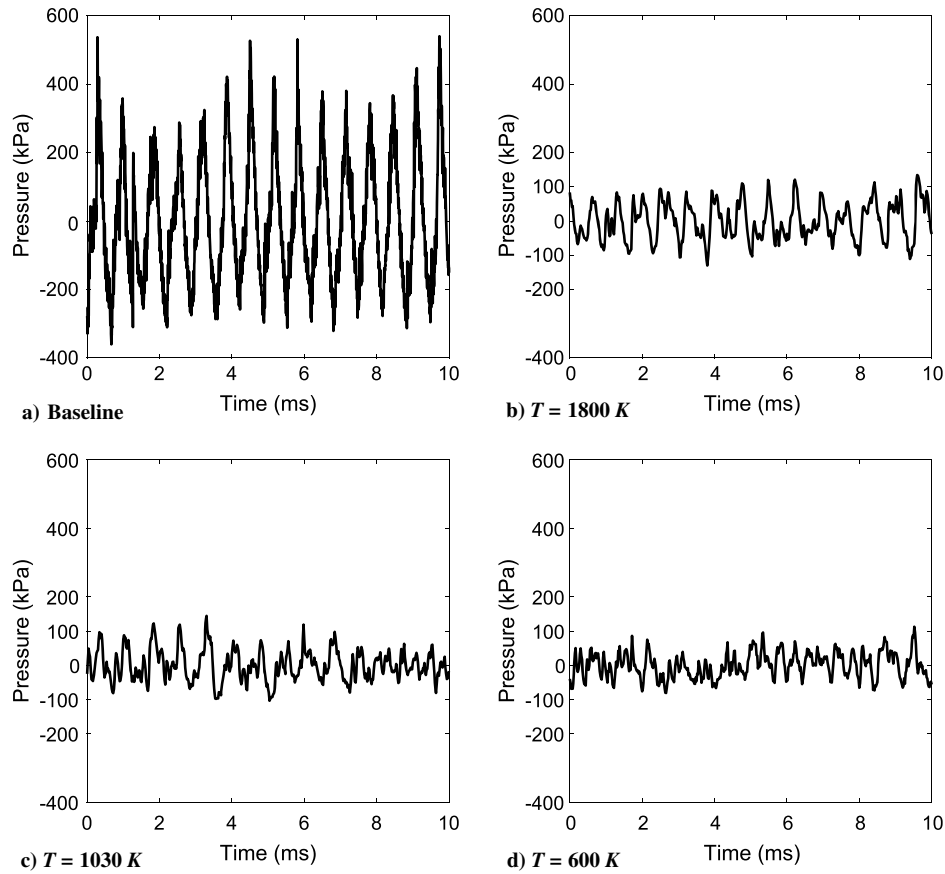


Fig. 7 Pressure signals on the combustion chamber wall at  $x = 37$  cm.

to the 1800 K case. The mean chamber pressure in the 600 K case is around 1700 kPa, with the mean to peak oscillation amplitude of about 75 kPa. Thus, it can be classified as stable. However, by computing the time-averaged fuel mass flow rate at the exit of the combustor, it is found that only around 42% of the fuel is unburned for the 600 K case. In comparison, 17.32 and 16.47% of the fuel is unburned for the 1030 and 1800 K, respectively. For the baseline (adiabatic) case, only 6% of the fuel exits the chamber unburned. These facts are consistent with previous findings [8] in which the instability enhanced the mixing process, leading to the much more efficient combustion processes. The stability achieved in the 600 K case results in inefficient burning.

Table 1 shows the frequency responses for the first three longitudinal modes for all the cases considered in this section. These frequencies are obtained by identifying the highest-frequency responses in the power spectral density (PSD) analyses. As seen in Table 1, decreases in the wall temperature lead to lower-frequency responses.

Figure 8 shows the first longitudinal-mode shape for all cases using the same postprocessing procedure described in Fig. 4b. The mode shape in these cases remains relatively the same but with much lower magnitudes.

Figure 9 shows the time-averaged temperatures as functions of the radial positions for all cases. The correct temperature values are found on the wall for each case, further confirming the validation of the new thermal boundary conditions. Although thermal boundary layers are

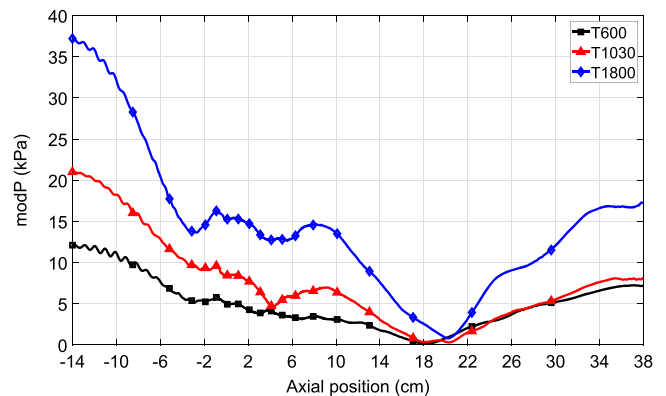


Fig. 8 First longitudinal-mode shape for all isothermal-wall cases.

seen in Fig. 9, their resolved structures, mainly through the laminar viscous sublayer, are questionable. This limitation is due to both the deficiency of the current turbulence model as well as the considerably coarse grids used for such high turbulence flow ( $Re \approx 400,000$ ). In reality, the actual combustor wall temperature through the viscous sublayer can be even lower than what is specified here as the wall temperature. Nevertheless, the importance of the isothermal boundary condition in modeling heat loss across the wall is shown in the current study.

Similar flame shapes are observed for all cases, with the most intense reactions found immediately downstream of the backstep in the shear layer and near the isothermal wall. Due to the heat loss at the wall, the flames in these cases are more compact around the backstep as compared to the baseline case. The right column of Fig. 10 shows the Rayleigh index [Eq. (18)] for all isothermal cases. These results are plotted using a scale that is an order of magnitude smaller than the baseline case (Fig. 6). Like the baseline case, there are favorable pressure–HRR couplings immediately downstream of the backstep

Table 1 Dominant frequencies on the combustion chamber wall at  $x = 37$  cm

Case	$f_1$ , Hz	$f_2$ , Hz	$f_3$ , Hz
Baseline	1520	3053	4565
$T = 1800$ K	1422	2670	4217
$T = 1030$ K	1397	2600	4017
$T = 600$ K	1372	2495	4017

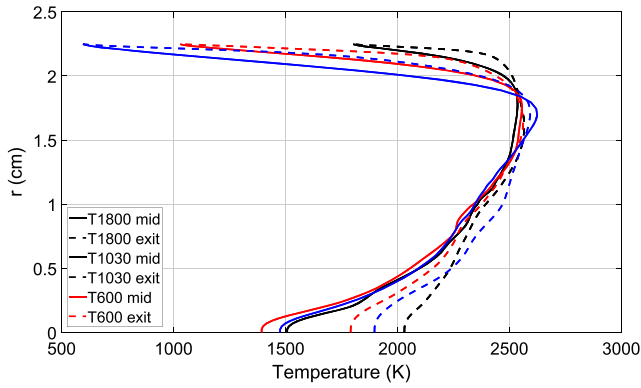


**Fig. 9** Time-averaged temperature at various axial locations for all cases. Solid lines represent streamwise midpoint (mid) of chamber, whereas broken lines represent exit location. Maximum y-axis value denotes combustion wall location.

in each case. However, there is a monotonic decrease in the pressure–HRR coupling observed, corresponding to a lower wall temperature, thus further confirming the stabilizing effect of the higher wall heat loss.

**C. Triggering**

The combustion instabilities occurring in all previous cases are self-excited. The remainder of this paper addresses the question of the nonlinear triggering instability. Both the fuel and oxygen mass flow rates are simultaneously perturbed to ensure a constant global equivalence ratio using the following general function:

$$\dot{m} = \dot{m}_i [1 + \epsilon(A_1 \sin(\omega_1 t) + A_2 \sin(\omega_2 t) + A_3 \sin(\omega_3 t))] \quad (19)$$

where  $m_i$  is either the fuel or oxidizer steady-state mass flow rate. Note that  $\omega_1, \omega_2,$  and  $\omega_3$  are the first-, second-, and third-mode frequencies for each respective case (Table 1). The effects of three different parameters associated with the perturbations are examined: amplitude, duration, and wave type. A global metric, defined as the triggered energy, is calculated to identify the threshold above which instability occurs. Descriptions of the combustion chamber transient responses to the perturbation are presented.

*1. Effects of Triggering Amplitudes*

In this section, propellant mass flow rates are modulated using a sine wave, which means  $A_1 = 1.0$ , whereas  $A_2$  and  $A_3$  are both zeros. The triggered duration corresponds to two periods of the first-mode frequency. Also,  $\epsilon$  is the nondimensional mean to peak oscillation amplitude, and it has three different values in this section: 0.25, 0.5, and 0.75. Figure 11 shows one type of the mass flow rate behavior at the propellant inlets, which is normalized by each propellant’s

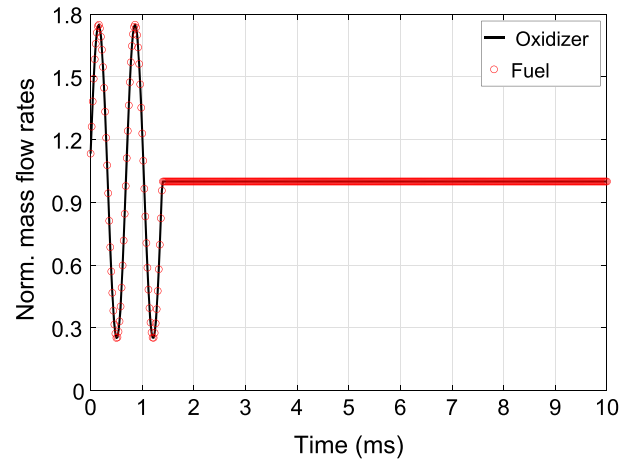


**Fig. 11** Propellant mass flow rate responses for  $\epsilon = 0.75$ : two-cycle sine wave.

steady-state mass flow rate. These signals are calculated from actual output data, indicating the correct triggered characteristics.

Figure 12 shows the pressure responses for the three cases. Even though the simulation time is 20 ms, only the first 10 ms are shown for clarity purposes. The perturbation occurs in the first 1.4 ms of the simulations. As seen in Fig. 12, an increase in perturbation amplitudes results in higher-pressure oscillations. Any disturbance amplitudes larger than 50% of the mean value quickly trigger the flowfield to higher-pressure amplitude oscillations. Limit-cycle behaviors are quickly established after the conclusion of the perturbation period. In the triggered cases ( $\epsilon > 0.5$ ), the steady-state limit-cycle amplitude is qualitatively the same, regardless of the strength of the initial disturbances. Due to the effect of heat loss across the chamber wall, these triggered amplitudes are still much smaller as compared to the baseline (adiabatic) case. Even though the disturbance frequency is exclusively in the first mode, PSD analyses of the limit-cycle pressure signals reveal that all three longitudinal modes are excited. Section III.C.3 further explores this particular phenomenon.

*2. Effects of Wave Types and Durations*

In this section, the effects of various wave types and durations are explored. Recalling Eq. (19), for a specific value of  $A_1, A_2$  and  $A_3$  are computed as

$$A_2 = \frac{2}{3}(1 - A_1), \quad A_3 = \frac{1}{3}(1 - A_1) \quad (20)$$

Two types of disturbances are explored: a pure sine wave in the first mode ( $A_1 = 1.0$ ), and a steep-fronted wave in which higher harmonics are superimposed ( $A_1 = 0.5$ ). Two different triggering

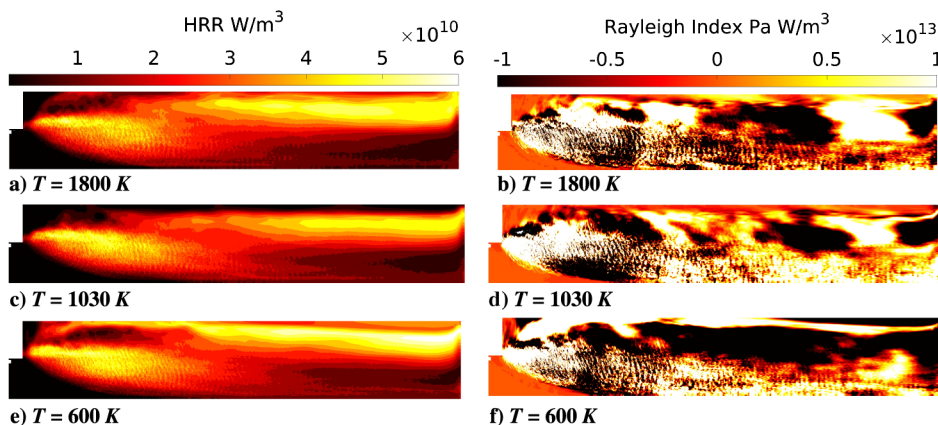


**Fig. 10** Time-averaged HRR (left column) and Rayleigh index (right column) for all the isothermal-wall cases.

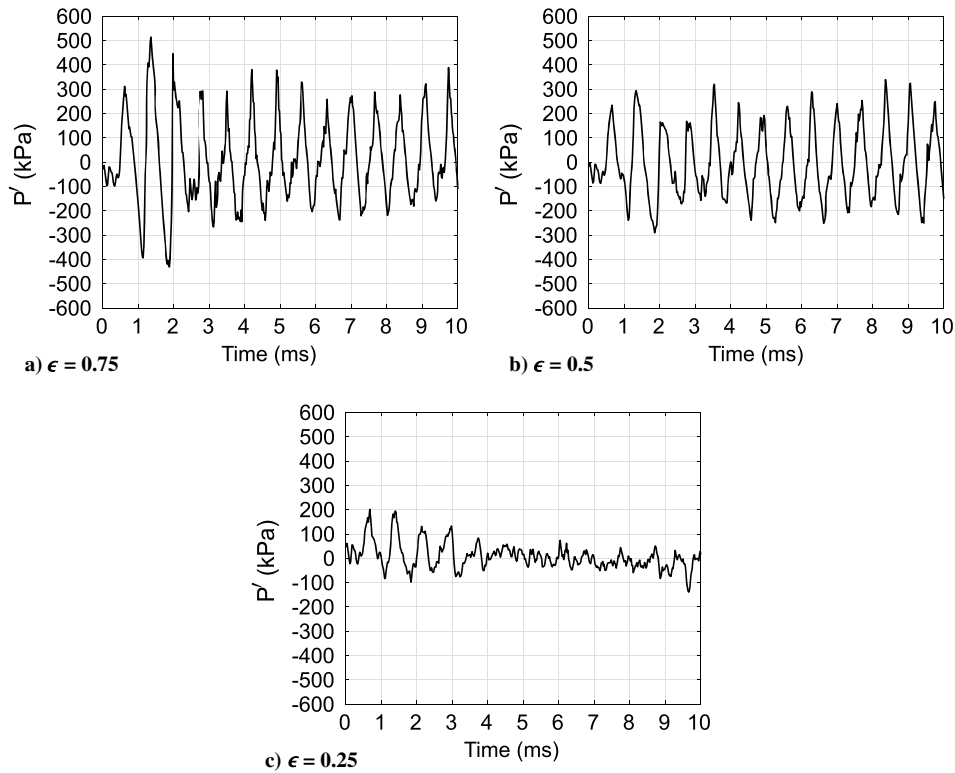


**Fig. 12** Pressure responses to different perturbation amplitudes. The signals are sampled on the chamber wall at  $x = 37$  cm.

durations, corresponding to two and four of the first-mode periods, are used for both wall conditions. Each simulation is again performed for 20 ms. Both the 1030 and 1800 K wall temperatures are used. Figure 13 shows the inlet normalized (Norm.) mass flow rate results for all four triggering simulations of the 1800 K case. Only the first 10 ms results are shown here for clarity.

Figures 14 and 15 show the pressure responses of the perturbed flow for both the 1800 and 1030 K cases. For both wall temperature

values, the longitudinal combustion instability is triggered for all cases except for the two-period steep wave. In all triggered cases, the limit-cycle amplitudes increase by a factor of two to three as compared to the stabilized cases. The triggered 1030 K cases' peak-to-peak oscillation amplitudes are roughly 100 kPa smaller than their 1800 K counterparts. Regardless of the type or duration of the disturbances, the limit-cycle magnitudes for the same wall temperature are qualitatively the same.

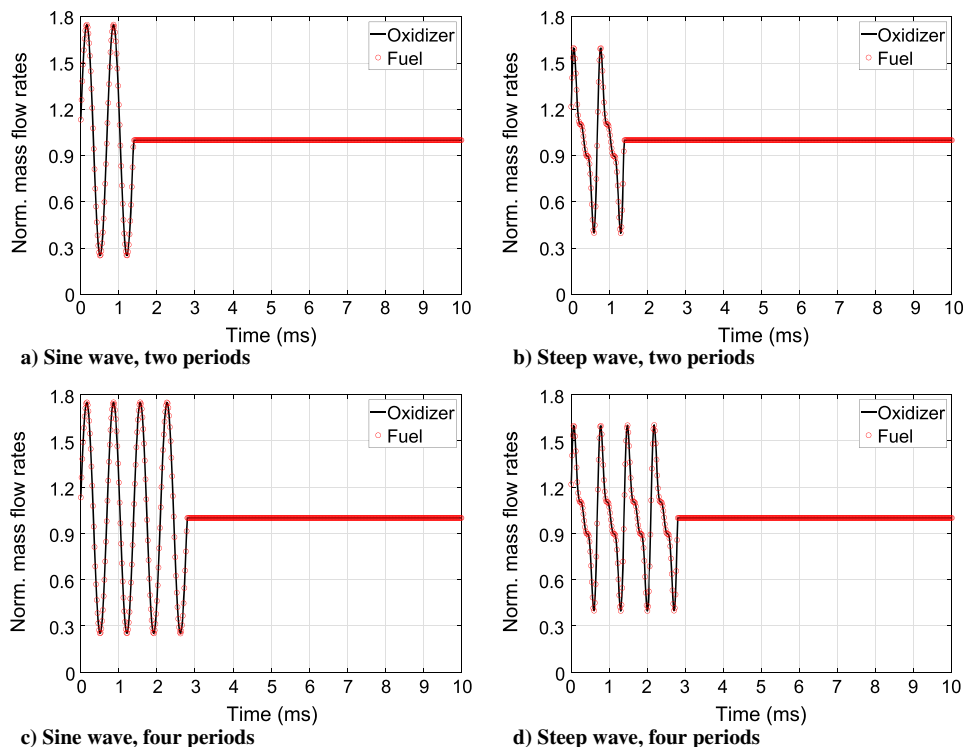


**Fig. 13** Normalized propellant mass flow rate results for cases with wall temperatures of 1800 K.

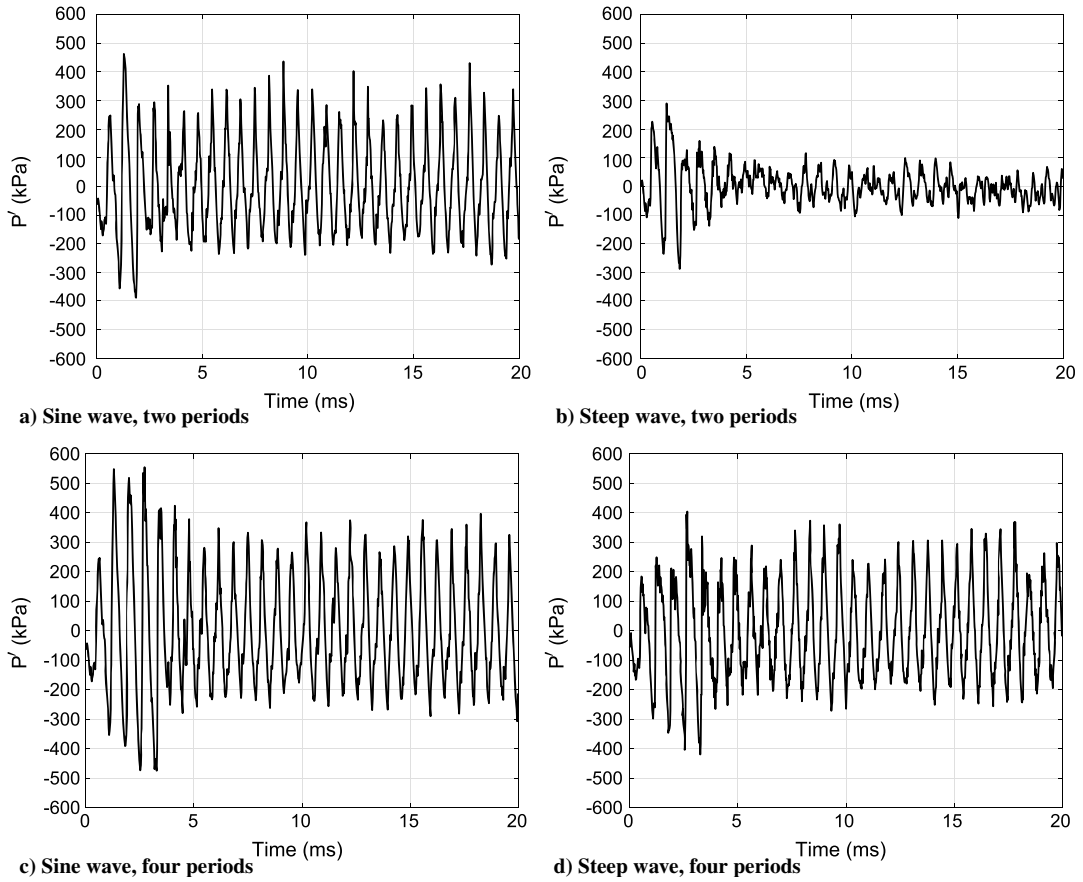


Fig. 14 Pressure responses for cases with wall temperatures of 1800 K at  $x = 37$  cm.

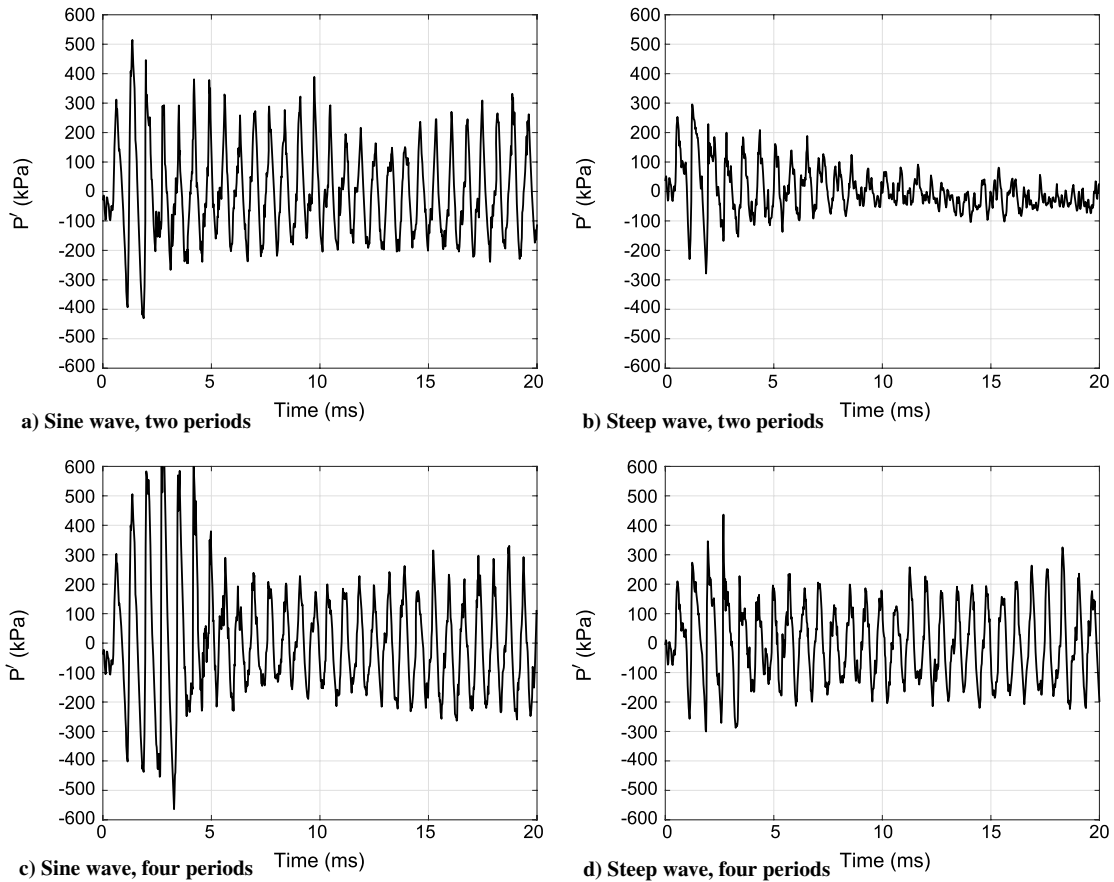


Fig. 15 Pressure responses for cases with wall temperatures of 1030 K at  $x = 37$  cm.

**Table 2** Triggered energy results for the 1030 K cases

$\epsilon$	Wave type	Periods	Triggered?	Triggered energy
0.25	Sine	2	No	0.065
0.5	Sine	2	Yes	0.262
0.75	Sine	2	Yes	0.588
0.75	Sine	4	Yes	1.176
0.75	Steep	2	No	0.228
0.75	Steep	4	Yes	0.457

Because of the nature of such a parametric study, as conducted here, it is useful to quantify the combined effect of perturbations on the combustion chamber. To that end, from Eq. (19), we formulate a new definition of triggered energy as

$$e_{\text{trig}} = \frac{\int_0^{\tau_{\text{trig}}} (\dot{m} - \dot{m}_s)^2 dt}{\dot{m}_s^2 T_{\text{trig}}} \quad (21)$$

where the nondimensional  $e_{\text{trig}}$  can be viewed as the cumulative mass flow rate triggered energy.  $T_{\text{trig}}$  is a single triggering period, which is calculated based on the first longitudinal-mode frequency. Note that  $\tau_{\text{trig}}$  is the total triggering duration, which is equal to either two or four times  $T_{\text{trig}}$ . Also,  $\dot{m}_s$  is the steady mass flow rate. For completeness, Table 2 only shows the results for the 1030 K cases, including the early effects of perturbation amplitudes.

There is a monotonic increase in maximum pressure responses that correspond to the monotonic increase in the triggered energy, as shown in the first 5 ms of Figs. 14 and 15. Evidently, if the triggered energy value is larger than 0.262, the semistable pressure oscillation in the chamber is excited to a new limit cycle with a higher amplitude. Obviously, the specific triggered energy definition used here should be modified based on the perturbation types introduced into the system. For further completeness, perturbation to the 600 K wall temperature is introduced using the most energetic disturbance (four-period sine wave with  $\epsilon = 0.75$ ). Figure 16 shows the pressure responses for this case. Even with the most energetic disturbance, the 600 K boundary condition provides sufficient heat loss across the chamber wall that the initial strong pressure response is effectively dampened. The initial pressure response, in this case, is much higher as compared to the 1030 and 1800 K cases due to the abundance of unburned fuel present within the combustion chamber. Therefore, the 600 K case is classified as unconditionally stable, whereas the unperturbed chamber with 1030 and 1800 K wall temperatures exhibits unstable limit-cycle or conditionally stable behaviors.

### 3. Instability Growth Mechanism

This section describes the transient responses of the chamber to the perturbations by examining how the introduction of the perturbation alters the combustion process. Because there are no significant differences in behaviors between the 1030 and 1800 K cases, we only

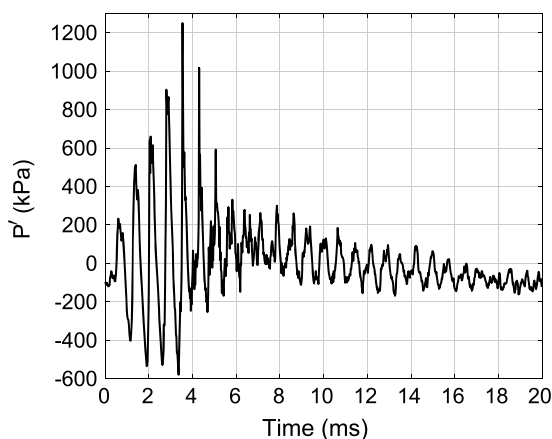


**Fig. 16** Pressure response of the 600 K wall temperature chamber using the four-period sine wave with  $\epsilon = 0.75$  disturbance.

present the 1800 K results for brevity purposes. Based on the results of the previous sections, the pressure–HRR coupling in the upstream pressure antinode region significantly contributes to driving the instability. Figure 17 shows the schematic of the upstream pressure antinode region, which is marked by the dotted vertical lines, henceforth referred to as region I. In the steady state after the disturbances conclude, the mass flow rates at injector inlets are held constant (Fig. 13). Therefore, to illustrate how the perturbations change the combustion process, the inlets of region I, which align axially with the splitter plane, are further examined.

Figures 18a–18d show the oxidizer and fuel mass flow rates across the two inlets of region I as functions of time, as defined by

$$m_i = 2\pi \int_{r_1}^{r_2} \bar{\rho}(r, t) \bar{u}(r, t) Y_i(r, t) r dr \quad (22)$$

These results are normalized by the injector inlet steady mass flow rates, which are 0.027 and 0.134 kg/s for the fuel and oxygen jets. The left column of Fig. 18 presents the sine wave results, whereas the right column shows the steep wave behaviors. Rapid injection of the propellants introduces more unburned reactants into this region during the first cycle for all cases. Moreover, the major surge in the propellant velocities due to the modulation rapidly enhances turbulent mixing of the unburned reactants. Subsequently, premixed burning significantly increases. As the oscillation amplitude increases, premixed burning also starts to grow. Based on our analysis using the flame index [7], premixed flames account for roughly 60 and 56% of the combustion process for the perturbed and unperturbed cases, respectively.

In Figs. 18a–18d, the curves with markers represent the two-period triggering duration, whereas the curves without any markers represent the four-period triggering duration. Each vertical broken line marks the conclusion of each triggering period. For all subfigures, the curves overlap each other during the first two triggering periods. The four-period waves show additional higher responses after the first two periods due to the continuations of mass flow modulations. For the entire duration of the triggering (e.g.,  $t = 0$ –1.4 ms for the two-period waves), the flow rates at the region I inlets respond identically to the perturbation waveforms. After the fourth period, the modulations stop for all cases. If the flow is triggered and the limit cycle is established (as seen in Figs. 14 and 15), the oxidizer jets in these cases exhibit steep-fronted wave behavior, dominated by the first longitudinal mode, regardless of the wave shape of the initial perturbation. The two-period steep wave curve shown in Fig. 18b eventually decays to the steady-state behavior of the unperturbed case. As observed in Figs. 18c and 18d, the fuel jets exhibit higher harmonics in the limit-cycle behavior even, when the initial disturbances are only in the first longitudinal sinusoidal mode, because the fuel port is not tuned to be in resonance with the

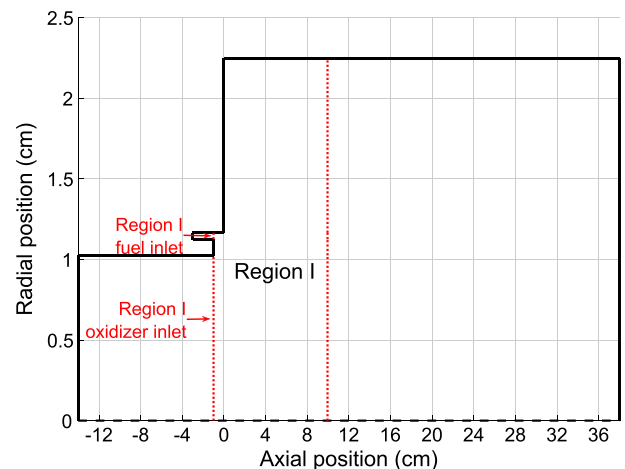


**Fig. 17** Schematic of the upstream pressure antinode region. The aspect ratio is not to scale.

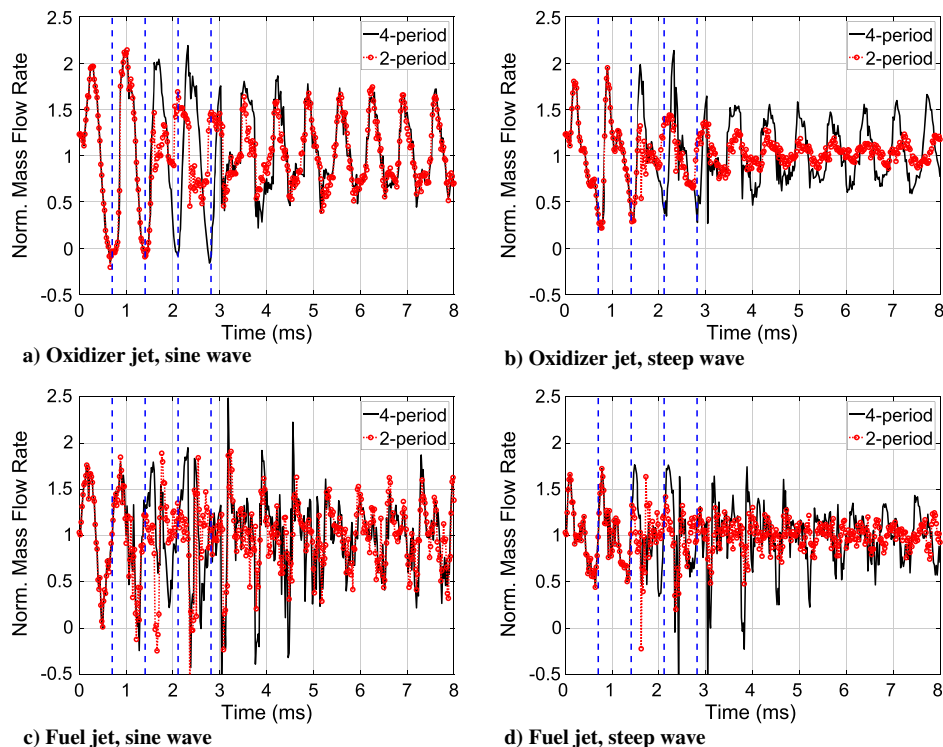


Fig. 18 Normalized reactant mass flow rates at inlet region I for the 1800 K cases. The vertical broken lines mark triggering periods.

combustion chamber. As seen from these figures, during the duration of the triggering, the perturbations in all cases, including the two-period steep wave case, reorganize the combustion processes by tuning it to the fundamental modes of the combustion chamber, leading to higher-pressure oscillations. However, once the disturbances are concluded, their cumulative magnitudes dictate whether the system reach a new higher dynamic equilibrium, as quantified by the triggered energy definition presented in the previous section. Evidently, when the cumulative strength of the disturbance is high enough to overcome the damping mechanism of the chamber, the flow reaches a new dynamic equilibrium with much higher limit-cycle oscillation amplitudes.

As seen from Fig. 18, after the perturbations conclude, in the triggered cases, the oscillations in the mass flow rates are caused by the pulsing mechanism, which is similar to ones found in self-excited instability. In this phenomenon, the adverse pressure gradient imposed by the upstream-running wave around the dump plane prohibits both propellants from entering region I, resulting in the trough of the mass flow vs time plot. Once the pressure wave passes the splitter plate, the flow accelerates and rapidly pushes the reactants into region I, reaching a peak of the entering mass flow. The newly injected reactants then combust in region I, subsequently raising the pressure of the volume, and the cycle repeats itself. A complete description of the pulsing mechanism is found in the work of Nguyen et al. [8]. Figures 19 and 20 compare the instantaneous HRR between the perturbed (and triggered) and unperturbed cases during their respective dynamic equilibrium for each wall temperature. For the perturbed cases, the HRR is plotted when the limit cycle is fully established. In each figure, the top row denotes the trough, whereas the bottom row denotes the peak of the pressure cycle within the upstream pressure anti-node region.

As observed from Figs. 19 and 20, the differences between the expansion and compression intervals are greater for the perturbed cases than for the unperturbed cases. These behaviors are analogous to those observed in the baseline case, which is shown in Fig. 5. There is, however, significantly more reaction immediately downstream of the backstep in the triggered 1800 K cases during the peak of the pressure cycle as compared to the 1030 K cases. This observation further confirms the lower triggered oscillation amplitudes of the 1030 K case.

Although the spatially local Rayleigh-index criterion, as shown in Figs. 6 and 10, is informative, it is not a quantitative approach that can adequately describe the triggering mechanism. Therefore, the Rayleigh index can be further extended as [40]

$$\frac{\gamma - 1}{\gamma p_o} \int_t \int_V p' q' dV dt > \int_t \int_S p' u' dS dt \quad (23)$$

where  $p'$ ,  $q'$ , and  $u'$  are the fluctuating pressure, HRR, and axial velocity. The left-hand side of the equation is the volume- and time-integrated definition of the spatially local Rayleigh index [Eq. (18)]. The right-hand side is defined as the net acoustic flux across the boundaries of the enclosed volume. For the instability to sustain (limit-cycle) or grow, the global Rayleigh index (RI) has to be larger than the net acoustic fluxes across the volume. Figure 21 shows the extended Rayleigh-index criterion for the upstream pressure antinode region ( $x = 0-10$  cm). Additionally, the total energy output for each region is plotted on the right secondary axes. The total energy output is defined as

$$E_{\text{out}} = \int_t \int_V \dot{\omega}_T dV dt \quad (24)$$

where  $\dot{\omega}_T$  is the instantaneous HRR and not the fluctuating HRR  $q'$ . This definition explains the difference in magnitudes between the total energy output and the correlation energy of the extended Rayleigh criterion.

As seen in Fig. 21, the first two cycles' data are the same for all quantities when comparing the results of the same wave type with differing durations, thereby indicating the consistency of the solver in obtaining the correct behavior. In all cases, the average energy output of the region remains the same. However, the correlation energy values are much as larger compared to the net acoustic fluxes across the volume for the triggered cases. To overcome the dampening factors of the combustion chamber, the lowest correlation energy at the conclusion of the disturbances is at least 12 J for all cases. Interestingly, despite the fact the maximum correlation energy for the four-period sine is as high as 40 J, the mean correlation energies in the new dynamic equilibrium are 13.54, 11.13, and 11.03 J for the four-period sine, two-period sine, and four-period steep wave cases. In

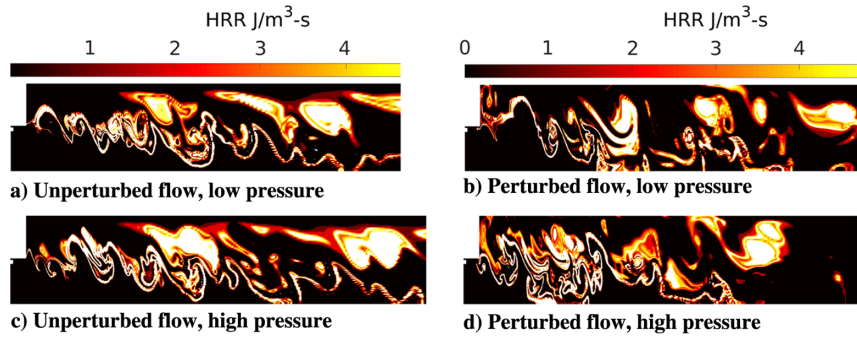


Fig. 19 Comparisons between the instantaneous HRRs of the unperturbed (left column) and triggered (right column) for the 1800 K case.

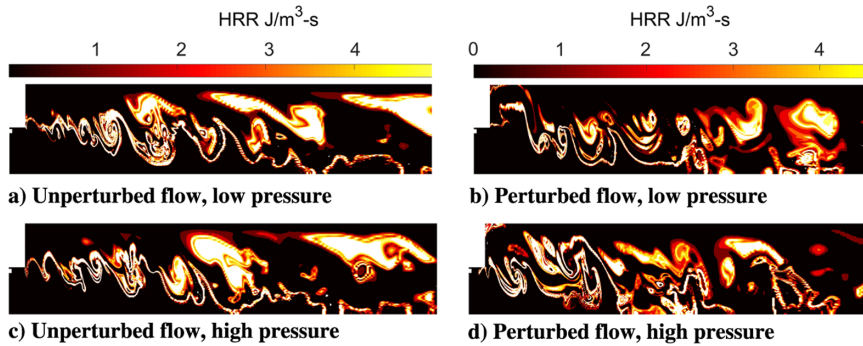


Fig. 20 Comparisons between the instantaneous HRRs of the unperturbed (left column) and triggered (right column) for the 1030 K case.

contrast, in the untriggered case (two-period steep wave), the correlation energy quickly decreases after the initial disturbance is concluded, leading to rapid decays of the initial pressure responses. The pressure–HRR coupling, and not the total energy output, is the dominating factor in determining if a new limit cycle is reached.

The Rayleigh index in Eq. (23), in the version defined by Nicoud and Poinot [40], takes a rather simplistic view in which the main criterion is the flame–acoustic coupling in a region that must be sufficiently strong to drive the acoustic fluxes across its enclosed value. The analysis in Fig. 21 identifies the strong flame–acoustic

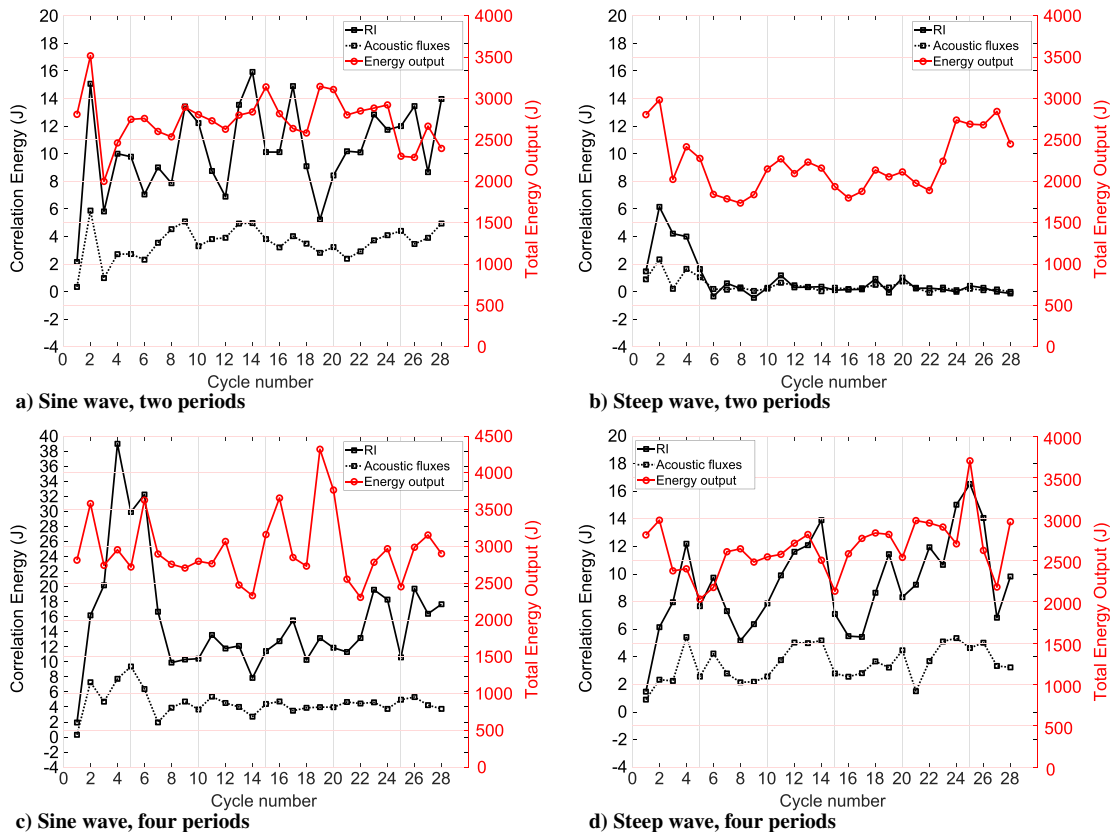


Fig. 21 Extended Rayleigh criterion results and total energy fluxes output of upstream pressure antinode for 1800 K cases. The y-axis ranges of Fig. 21c are larger as compared to the other three subfigures.

coupling in region I as the main driving mechanism that excites the pressure oscillations to a higher limit-cycle behavior. Therefore, it should not be used to represent the whole chamber behavior. As the acoustic fluxes exit region I, they can encounter other dissipation mechanisms such as viscous damping. Additionally, the flow also heads toward a pressure node and velocity antinode, which can also have dampening effects. Therefore, a more reasonable expectation is that the chamber, through dynamic equilibrium, eventually reaches a higher limit-cycle behavior.

#### IV. Conclusions

Combustion chamber stabilizing effects are explored by introducing heat loss across the combustion chamber wall. Isothermal-wall boundary conditions with different temperatures are used (1800, 1030, and 600 K). Compared to the adiabatic case in which the wall temperature is 2700 K, imposing an 1800 K wall produces significant heat loss. A further decrease in wall temperature results in more modest amplitude reduction. There is a monotonic decrease in oscillation amplitudes as the wall temperature decreases. The 600 K wall temperature results in stable oscillation. As the pressure oscillation amplitude decreases, there is more unburned fuel escaping the chamber. Therefore, stabilizing the chamber using heat loss is not desirable due to the inefficient combustion process.

The triggering instability for the stabilized chamber is subsequently simulated. Realistic chamber cooling requires a lower wall temperature than some values used here. However, for the current turbulent boundary layers, these imposed values should be larger than expected values inside the laminar sublayer. Triggering is achieved by perturbing the mass flow rate at the inlet for a limited duration. Both the fuel and oxidizer mass flow are simultaneously disturbed to maintain a constant global equivalence ratio. Two different types of disturbance, with two different perturbation periods, are considered: sine and steep waves. A total of eight simulations are performed. For the steep wave with two periods of perturbation, the sizable initial pressure response quickly decays, regardless of the wall temperature. Triggered instability occurs for the sine wave with various durations and a steep wave with four periods of perturbation. In all cases, the pressure oscillation amplitudes increase by at least a factor of two. A threshold for triggered energy is identified; above which, combustion instability is triggered regardless of the disturbance types. For both wall temperatures of 1800 and 1030 K, the triggered limit-cycle amplitudes are the same, regardless of the initial triggered energy magnitudes. These findings are consistent with results obtained by Levine and Baum [13] for the solid-rocket motor. The perturbation demonstrates that, by forcing the propellant mass flow rates, the pressure-HRR coupling is subsequently forced at the upstream pressure antinode region to be in phase. As a direct result, the reactant flows that exit the injector and enter the combustion chamber exhibit coherent unstable oscillatory behaviors after the injector mass flow rates return to steady state. The trigger has forced a new organization of the mean burning process that results in larger-amplitude oscillations. The findings here are very useful during the design process, especially when it comes to classifying the stability of the combustion chamber.

#### Acknowledgments

This research is supported by the U.S. Air Force Office of Scientific Research under grant FA9550-18-1-0392 with Mitat Birkan as the Scientific Manager. Heinz Pitsch of RWTH Aachen University is acknowledged for providing us access to the FlameMaster code.

#### References

- [1] Culick, F. E., "Unsteady Motions in Combustion Chambers for Propulsion Systems," AGARDograph, AG-AVT-039, Neuilly-Sur-Seine, France, 2006.
- [2] Sirignano, W. A., and Popov, P., "Two-Dimensional Model for Liquid-Rocket Transverse Combustion Instability," *AIAA Journal*, Vol. 51, No. 12, 2013, pp. 2919–2934. doi:10.2514/1.J052512
- [3] Miller, K., Sisco, J., Nugent, N., and Anderson, W., "Combustion Instability with a Single Element Swirl Injector," *Journal of Propulsion and Power*, Vol. 23, No. 5, 2007, pp. 1102–1112. doi:10.2514/1.26826
- [4] Yu, Y. C., Koeglmeier, S. M., Sisco, J. C., and Anderson, W. E., "Combustion Instability of Gaseous Fuels in a Continuously Variable Resonance Chamber (CVRC)," *44th AIAA/ASME/SAE/ASEE Joint Propulsion Conference and Exhibit*, AIAA Paper 2008-4657, 2008. doi:10.2514/6.2008-4657
- [5] Yu, Y. C., O'Hara, L., Sisco, J. C., and Anderson, W. E., "Experimental Study of High-Frequency Combustion Instability in a Continuously Variable Resonance Combustor(CVRC)," *47th AIAA Aerospace Sciences Meeting Including the New Horizons Forum and Aerospace Exposition*, AIAA Paper 2009-234, 2009. doi:10.2514/6.2009-234
- [6] Yu, Y. C., Sisco, J. C., Rosen, S., Madhav, A., and Anderson, W. E., "Spontaneous Longitudinal Combustion Instability in a Continuously Variable Resonance Combustor," *Journal of Propulsion and Power*, Vol. 28, No. 5, 2012, pp. 876–887. doi:10.2514/1.B34308
- [7] Nguyen, T. M., and Sirignano, W. A., "The Impacts of Three Flamelet Burning Regimes in Nonlinear Combustion Dynamics," *Combustion and Flame*, Vol. 195, Sept. 2018, pp. 170–182. doi:10.1016/j.combustflame.2018.03.031
- [8] Nguyen, T. M., Popov, P. P., and Sirignano, W. A., "Longitudinal Combustion Instability in a Rocket Engine with a Single Coaxial Injector," *Journal of Propulsion and Power*, Vol. 34, No. 2, 2018, pp. 354–373. doi:10.2514/1.B36516
- [9] Srinivasan, S., Ranjan, R., and Menon, S., "Flame Dynamics During Combustion Instability in a High-Pressure, Shear-Coaxial Injector Combustor," *Flow, Turbulence and Combustion*, Vol. 94, No. 1, 2015, pp. 237–262. doi:10.1007/s10494-014-9569-x
- [10] Harvazinski, M. E., Anderson, W. E., and Merkle, C. L., "Analysis of Self-Excited Combustion Instabilities Using Two- and Three Dimensional Simulations," *Journal of Propulsion and Power*, Vol. 29, No. 2, 2013, pp. 396–409. doi:10.2514/1.B34732
- [11] Harvazinski, M., Huang, C., Sankaran, V., Feldman, T., Anderson, W., Merkle, C., and Talley, D., "Coupling Between Hydrodynamics, Acoustics, and Heat Release in a Self-Excited Unstable Combustor," *Physics of Fluids*, Vol. 27, No. 4, 2015, Paper 045102. doi:10.1063/1.4916673
- [12] Garby, R., Selle, L., and Poinso, T., "Large-Eddy Simulation of Combustion Instabilities in a Variable Length Combustor," *Comptes Rendus Mecanique*, Vol. 341, Nos. 1–4, 2013, pp. 220–229. doi:10.1016/j.crme.2012.10.020
- [13] Levine, J. N., and Baum, J. D., "A Numerical Study of Nonlinear Instability Phenomena in Solid Rocket Motors," *AIAA Journal*, Vol. 21, No. 4, 1983, pp. 557–564. doi:10.2514/3.8113
- [14] Baum, J. D., and Levine, J. N., "Modeling of Nonlinear Longitudinal Instability in Solid Rocket Motors," *Acta Astronautica*, Vol. 13, Nos. 6–7, 1986, pp. 339–348. doi:10.1016/0094-5765(86)90089-5
- [15] Wicker, J. M., Greene, W. D., Kim, S.-I., and Yang, V., "Triggering of Longitudinal Combustion Instabilities in Rocket Motors: Nonlinear Combustion Response," *Journal of Propulsion and Power*, Vol. 12, No. 6, 1996, pp. 1148–1158. doi:10.2514/3.24155
- [16] Urbano, A., Selle, L., Staffebach, G., Cuenot, B., Schmitt, T., Ducruix, S., and Candel, S., "Exploration of Combustion Instability Triggering Using Large Eddy Simulation of a Multiple Injector Liquid Rocket Engine," *Combustion and Flame*, Vol. 169, July 2016, pp. 129–140. doi:10.1016/j.combustflame.2016.03.020
- [17] Popov, P. P., Sideris, A., and Sirignano, W. A., "Stochastic Modeling of Transverse Wave Instability in a Liquid-Propellant Rocket Engine," *Journal of Fluid Mechanics*, Vol. 745, April 2014, pp. 62–91. doi:10.1017/jfm.2014.96
- [18] Popov, P. P., Sirignano, W. A., and Sideris, A., "Propellant Injector Influence on Liquid-Propellant Rocket Engine Instability," *Journal of Propulsion and Power*, Vol. 31, No. 1, 2015, pp. 320–331. doi:10.2514/1.B35400
- [19] Popov, P. P., Sideris, A., and Sirignano, W. A., "Triggering and Restabilization of Combustion Instability with Rocket Motor Acceleration," *AIAA Journal*, Vol. 54, No. 5, 2016, pp. 1652–1659. doi:10.2514/1.J054542

- [20] Popov, P. P., Sideris, A., and Sirignano, W. A., "Low-Probability Events Leading to Rocket Engine Combustion Instability," *AIAA Journal*, Vol. 55, No. 3, 2017, pp. 919–929.  
doi:10.2514/1.J055276
- [21] Sirignano, W. A., "Theoretical Study of Nonlinear Combustion Instability: Longitudinal Mode," Ph.D. Thesis, Dept. of Aerospace and Mechanical Sciences, Princeton Univ., Princeton, NJ, 1964.
- [22] Mitchell, C. E., Crocco, L., and Sirignano, W. A., "Nonlinear Longitudinal Instability in Rocket Motors with Concentrated Combustion," *Combustion Science and Technology*, Vol. 1, No. 1, 1969, pp. 35–64.  
doi:10.1080/00102206908952190
- [23] Yang, V., Kim, S., and Culick, F. E., "Triggering of Longitudinal Pressure Oscillations in Combustion Chambers. I: Nonlinear Gas Dynamics," *Combustion Science and Technology*, Vol. 72, Nos. 4–6, 1990, pp. 183–214.  
doi:10.1080/00102209008951647
- [24] Lores, M. E., and Zinn, B. T., "Nonlinear Longitudinal Combustion Instability in Rocket Motors," *Combustion Science and Technology*, Vol. 7, No. 6, 1973, pp. 245–256.  
doi:10.1080/00102207308952365
- [25] Garby, R., Selle, L., and Poinso, T., "Analysis of the Impact of Heat Losses on an Unstable Model Rocket-Engine Combustor Using Large-Eddy Simulation," *48th AIAA/ASME/SAE/ASEE Joint Propulsion Conference and Exhibit*, AIAA Paper 2012-4085, 2012.  
doi:10.2514/6.2012-4085
- [26] Harvazinski, M., Sankaran, V., and Talley, D., "Parametric Trends in the Combustion Stability Characteristics of a Single-Element Gas-Gas Rocket Engine," *52nd AIAA Aerospace Sciences Meeting*, AIAA Paper 2014-0577, 2014.  
doi:10.2514/6.2014-0577
- [27] Sardeshmukh, S. V., Heister, S. D., and Anderson, W. E., "Prediction of Combustion Instability with Detailed Chemical Kinetics," *53rd AIAA Aerospace Sciences Meeting*, AIAA Paper 2015-1826, 2015.  
doi:10.2514/6.2015-1826
- [28] Frenklach, M., Wang, H., and Yu, C.-L., et al., "GRI-Mech—An Optimized Detailed Chemical Reaction Mechanism for Methane Combustion," Rept. GRI-95/0058, Nov. 1995, [http://www.me.berkeley.edu/gri\\_mech/](http://www.me.berkeley.edu/gri_mech/).
- [29] Jameson, A., Schmidt, W., and Turkel, E., "Numerical Solution of the Euler Equations by Finite Volume Methods Using Runge Kutta Time Stepping Schemes," *14th Fluid and Plasma Dynamics Conference*, AIAA Paper 1981-1259, 1981.  
doi:10.2514/6.1981-1259
- [30] Pecnik, R., Terrapon, V. E., Ham, F., Iaccarino, G., and Pitsch, H., "Reynolds-Averaged Navier–Stokes Simulations of the Hyshot II Scramjet," *AIAA Journal*, Vol. 50, No. 8, 2012, pp. 1717–1732.  
doi:10.2514/1.J051473
- [31] Wilcox, D. C., *Turbulence Modelling for CFD*, 3rd ed., DCW Industries, Inc., La Cañada, CA, 2006, pp. 255–256.
- [32] Strelets, M., "Detached Eddy Simulation of Massively Separated Flows," *39th Aerospace Sciences Meeting and Exhibit*, AIAA Paper 2001-879, 2001.  
doi:10.2514/6.2001-879
- [33] Nichols, R. H., "A Comparison of Hybrid RANS/LES Turbulence Models for a Generic Weapons Bay with and Without a Spoiler," *26th AIAA Applied Aerodynamics Conference*, AIAA Paper 2008-6229, 2008.  
doi:10.2514/6.2008-6229
- [34] Saghafian, A., Shunn, L., Phillip, D. A., and Ham, F., "Large Eddy Simulations of the HIFiRE Scramjet Using a Compressible Flamelet/Progress Variable Approach," *Proceedings of the Combustion Institute*, Vol. 35, No. 2, 2015, pp. 2163–2172.  
doi:10.1016/j.proci.2014.10.004
- [35] Echehki, T., and Mastorakos, E., *Turbulent Combustion Modeling*, Vol. 95, Fluid Mechanics and Its Applications, 1st ed., Springer, New York, 2011, Chap. 3.
- [36] Ma, P. C., Wu, H., Ihme, M., and Hickey, J.-P., "A Flamelet Model with Heat-Loss Effects for Predicting Wall-Heat Transfer in Rocket Engines," *53rd AIAA/SAE/ASEE Joint Propulsion Conference*, AIAA Paper 2017-4856, 2017.  
doi:10.2514/6.2017-4856
- [37] Poinso, T., and Veynante, D., *Theoretical and Numerical Combustion*, 2nd ed., R.T. Edwards, Philadelphia, PA, 2005, pp. 433–456.
- [38] Crocco, L., and Sirignano, W. A., "Effects of Transverse Velocity Components on the Nonlinear Behavior of Short Nozzles," *AIAA Journal*, Vol. 4, No. 8, 1966, pp. 1428–1430.  
doi:10.2514/3.3691
- [39] Nguyen, T. M., "Nonlinear Rocket-Engine Longitudinal Combustion Instabilities," Ph.D. Thesis, Univ. of California, Irvine, CA, 2018.
- [40] Nicoud, F., and Poinso, T., "Thermoacoustic Instabilities: Should the Rayleigh Criterion Be Extended to Include Entropy Changes," *Combustion and Flame*, Vol. 142, Nos. 1–2, 2005, pp. 153–159.  
doi:10.1016/j.combustflame.2005.02.013

J. P. Drummond  
Associate Editor